Journal of Materials Chemistry A

DFT Screening of Dual-atom Catalysts on Carbon Nanotubes for Enhanced Oxygen Reduction Reaction and Oxygen Evolution Reaction: Comparing Dissociative and Associative Mechanisms

Journal:	*Journal of Materials Chemistry A*
Manuscript ID	TA-ART-05-2024-003519.R1
Article Type:	Paper
Date Submitted by the Author:	19-Aug-2024
Complete List of Authors:	Zhou, Xiangyi; The University of Hong Kong Tamtaji, Mohsen; Hong Kong Quantum AI Lab Limited Zhou, Weijun; QuantumFabless Limited Goddard III, William; California Institute of Technology Chen, Guanhua; The University of Hong Kong,

DFT Screening of Dual-atom Catalysts on Carbon Nanotubes for Enhanced Oxygen Reduction Reaction and Oxygen Evolution Reaction: Comparing Dissociative and Associative Mechanisms

Xiangyi Zhou[1], Mohsen Tamtaji[2], Weijun Zhou[3], William A. Goddard III[4]*, Guanhua Chen[1,2,3]*

[1]*Department of Chemistry, The University of Hong Kong, Pokfulam Road, Hong Kong SAR, China*

[2]*Hong Kong Quantum AI Lab Limited, Pak Shek Kok, Hong Kong SAR, China*

[3]*QuantumFabless Limited, Pak Shek Kok, Hong Kong SAR, China*

[4]*Materials and Process Simulation Center (MSC), MC 139-74, California Institute of Technology, Pasadena CA, 91125, USA*

*Corresponding Authors, email: ghc@everest.hku.hk, and wag@caltech.edu

ORCID: XYZ: 0009-0002-8311-0768; MT: 0000-0001-9118-5474; WJZ: 0000-0002-4328-3704; WAG: 0000-0003-0097-5716; GHC: 0000-0001-5015-0902

Abstract

Dual-atom catalysts (DACs) are promising for the oxygen reduction reaction (ORR) and the oxygen evolution reaction (OER). However, two vital factors, namely curvature effects and dissociative mechanisms, are often overlooked in DAC studies, which may miss the possibility of finding the most promising candidates. To provide the mechanistic understanding of the role of these two essential factors in effective electrocatalyst design, we explore systematically the catalytic potential of $MM'N_6$-DACs supported on graphene and single-walled carbon nanotubes (CNTs) with two diameters within both dissociative and associative mechanisms where M and M′ represent Fe, Co, Ni, Cu, Ru, Rh, Pd, or Pt metals. More than ten DACs have shown high activity with overpotential lower than common commercial catalysts, notably non-precious $CoCuN_6$-DACs exhibiting extremely low ORR overpotential of 0.09 V_{RHE} and low OER overpotential of 0.10 V_{RHE}, and bifunctional ORR and OER overpotential of 0.22 V_{RHE}. We find that CNT substrates gradually strengthen the adsorption of intermediates on $CoCuN_6$-DACs compared to graphene substrate, due to increased electronic density of states of metal atoms near the Fermi level. The dissociative mechanism circumvents the constraints of scaling relationship in the associative mechanism, so that several DACs favoring the dissociative mechanism exhibit substantially improved activity, with lower overpotential than the theoretical minimum of the associative mechanism. These results not only shed light on designing high-performance catalysts for ORR and OER, but also deepen the theoretical understanding of catalytic mechanism and curvature effects on DACs.

Keywords: Curvature effects, reaction mechanisms, breaking scaling relationship, theoretical insights, oxygen electrocatalysis, metal-air batteries

1. Introduction

The Oxygen Reduction Reaction (ORR) and the Oxygen Evolution Reaction (OER) involving transformations between water and oxygen, are crucial for (rechargeable) metal-air batteries, fuel cells, and electrolyzers[1–6]. Particularly, in the oxygen electrode of rechargeable metal-air batteries, both reactions are important. These sluggish reactions require catalysts to boost their rate[7]. Currently, popular commercial catalysts for ORR and OER are based on bulk Pt [8,9] and RuO_2 [10,11], respectively, which are hampered by their high cost and only medium activity. Therefore, developing replacements combining economic viability with superior performance for these precious catalysts is an urgent and important challenge. Especially, bifunctional catalysts capable of catalyzing both reactions are essential for improving rechargeable metal-air batteries.

Designing atomically dispersed metal catalysts, such as single atom catalysts (SACs) [12–18] and dual-atom catalysts (DACs) [19,20], is widely regarded as a promising strategy to replace the need for high-cost Pt and RuO_2 catalysts to achieve reliable activity and reduce cost by ultra-high metal utilization. Significant theoretical and experimental efforts have been devoted to exploring potential SACs for various electrocatalytic processes, such as ORR[21–26], OER[22,25], the N_2 reduction reaction (N_2RR)[27], and the CO_2 reduction reaction (CO_2RR)[28–30]. However, these reactions involve multiple intermediates, whereas the activity of SACs is severely limited by the scaling relationship between intermediates. By contrast, DACs have the potential to outperform SAC performance due to possible synergy between two active sites [31–33]. For example, more than ten metallic dimers anchored by 6 pyridine nitrogen-doped graphene have shown excellent OER activity, outperforming their corresponding SACs [34].

ORR and OER can take place through both dissociative and associative mechanisms. Most of the existing research on DACs for mono- and bi-functional oxygen electrocatalysis consider only their performance for the associative mechanism in planar configuration, without considering curvature effects or the dissociative mechanism. However, these two factors may play a key role in designing effective DACs. Studies have shown that curvature effects can be utilized to adjust the activity of SACs for various electrocatalysis[35–42] and CoCo-DACs for oxygen electrocatalysis [43]. In addition, some recent studies have shown that oxygen electrocatalysis on DACs may favor dissociative mechanism due to the synergy of dual atoms[34,43,44]. Therefore, to address the lack of DAC screening for oxygen electrocatalysis that considers curvature and dissociation, we conducted a systematic screening for mono- and bi-functional ORR/OER catalysts, incorporating these critical factors.

Herein, in the hope of finding the best DACs for oxygen electrocatalysis, we theoretically investigated ORR and OER performance of $MM'N_6$-DACs in 3 curvature conditions for both the dissociative and associative mechanisms, where M and M′ represent Fe, Co, Ni, Cu, Ru, Rh, Pd, or Pt metals. Dual-atom sites on graphene represent the planar condition (noted as $d = \infty$ nm), while these sites on carbon nanotubes (CNTs) with two diameters (d) represent two curved conditions (i.e. d = 1.3 nm, and d = 0.8 nm). We found some promising catalysts for mono- and bi-functional oxygen electrocatalysis with ultra-low overpotential especially in dissociative mechanism, such as

- $CoCu_{d=\infty\ nm}$-DAC (with ORR overpotential η^{ORR} = 0.09 V, OER overpotential η^{OER} = 0.13 V, and bifunctional ORR and OER overpotential $\eta^{bifunc} = \eta^{ORR} + \eta^{OER}$ = 0.09 + 0.13 = 0.22 V) and
- $CoCu_{d=1.3\ nm}$-DAC (with η^{ORR} = 0.22 V, η^{OER} = 0.10 V, and $\eta^{bifunc} = \eta^{ORR} + \eta^{OER}$ = 0.22 + 0.10 = 0.32 V).

Moreover, unlike the tethered performance dictated by scaling relationships in associative mechanism, the dissociative pathway in oxygen electrocatalysis offers a novel possibility for catalyst activity free from the above limitations. We analyze the curvature effects on the adsorption of intermediates on $CoCuN_6$-DACs and discuss the electronic origin.

2. Methods

2.1 Dissociative and Associative Mechanisms of ORR and OER

ORR transferring four electron and protons can be expressed as follows:

$$O_2 + 4\,(H^+ + e^-) \rightarrow 2H_2O \quad E^\circ = 1.23V \tag{1}$$

ORR can go in either dissociative mechanism or associative mechanism. Four steps of dissociative mechanism can be expressed as:

$$2* + O_2 + (H^+ + e^-) \rightarrow *O + *OH \tag{2}$$

$$*O + *OH + (H^+ + e^-) \rightarrow *O + * + H_2O \tag{3}$$

$$*O + * + (H^+ + e^-) \rightarrow *OH + * \tag{4}$$

$$*OH + * + (H^+ + e^-) \rightarrow 2* + H_2O, \tag{5}$$

while those of associative mechanism can be expressed as:

$$* + O_2 + (H^+ + e^-) \rightarrow *OOH \tag{6}$$

$$*OOH + (H^+ + e^-) \rightarrow *O + H_2O \tag{7}$$

$$*O + (H^+ + e^-) \rightarrow *OH \tag{8}$$

$$*OH + (H^+ + e^-) \rightarrow * + H_2O, \tag{9}$$

where $*$ represents the adsorption site. OER is regarded as the reverse reaction of ORR.

For dissociative mechanism, the adsorption free energies (ΔG) of intermediates were calculated as:

$$\Delta G_{*O/*OH} = G_{*O/*OH} - G_{*} + \frac{3}{2}G_{H_2} - 2G_{H_2O} - 3eU \quad (10)$$

$$\Delta G_{*OH/*OH} = G_{*OH/*OH} - G_{*} + G_{H_2} - 2G_{H_2O} - 2eU \quad (11)$$

$$\Delta G_{*OH} = G_{*OH} - G_{*} + \frac{1}{2}G_{H_2} - G_{H_2O} - eU. \quad (12)$$

By contrast, for associative mechanism,

$$\Delta G_{*OOH} = G_{*OOH} - G_{*} + \frac{3}{2}G_{H_2} - 2G_{H_2O} - 3eU \quad (13)$$

$$\Delta G_{*O} = G_{*O} - G_{*} + G_{H_2} - G_{H_2O} - 2eU \quad (14)$$

$$\Delta G_{*OH} = G_{*OH} - G_{*} + \frac{1}{2}G_{H_2} - G_{H_2O} - eU. \quad (15)$$

The energy of ($H^+ + e^-$) at potential U was obtained through the computational hydrogen electrode (CHE) model as $\frac{1}{2}G_{H_2} - eU$.

2.2 Computational details

All spin-polarized density functional theory (DFT) calculations were performed using VASP 6.1.0. The exchange-correlation functional was Perdew−Burke−Ernzerhof (PBE) based on the generalized gradient approximation (GGA) with a plane-wave cutoff energy of 500 eV[45–48]. Van der Waals interactions were included using the Grimme D3 method[49,50]. VASPsol was used to simulate the implicit solvation effect of water [51,52].

A vacuum space of 15 Å was employed to avoid interactions between two adjacent periodic images for all structure models. For structural models based on graphene, the Brillouin zone was sampled with 3×1×4 and 5×1×7 *k*-points grids based on the Monkhorst–Pack scheme for structural optimization and single-point energy

calculations, respectively. For structural models based on carbon nanotubes, *k*-points grids were 1×1×4 and 1×1×7, respectively. The convergence thresholds for force and electronic structure energy were 0.02 eV/Å and 10^{-5} eV[53], respectively.

For each elementary step in oxygen electrocatalysis, the computational hydrogen electrode (CHE) model was employed to compute the Gibbs free energy change (ΔG) as[54]:

$$\Delta G = \Delta E + \Delta ZPE - T\Delta S \quad (16)$$

Where, ΔE is the electronic energy difference, ΔZPE is the zero-point energy, T is the temperature (298.15 K), and ΔS is the entropy corrections.

The theoretical onset potential and overpotential were calculated from ΔG of intermediates in the elementary reaction steps. In the dissociative mechanism, the onset potential of ORR and OER was calculated as:

$$U_{ORR}^{onset} = -\max\{(\Delta G_{*O/*OH} - 4.92), (\Delta G_{*OH/*OH} - \Delta G_{*O/*OH}), (\Delta G_{*OH} - \Delta G_{*OH/*} \quad (17)$$
$$/e$$

$$U_{OER}^{onset} = -\max\{(4.92 - \Delta G_{*O/*OH}), (\Delta G_{*O/*OH} - \Delta G_{*OH/*OH}), (\Delta G_{*OH/*OH} - \Delta G \quad (18)$$
$$/e$$

By contrast, in the associative mechanism, the onset potential of ORR and OER was calculated as:

$$U_{ORR}^{onset} = -\max\{(\Delta G_{*OOH} - 4.92), (\Delta G_{*O} - \Delta G_{*OOH}), (\Delta G_{*OH} - \Delta G_{*O}), (-\Delta G_{*OH}) \quad (19)$$

$$U_{OER}^{onset} = -\max\{(4.92 - \Delta G_{*OOH}), (\Delta G_{*OOH} - \Delta G_{*O}), (\Delta G_{*O} - \Delta G_{*OH}), (\Delta G_{*OH})\} \quad (20)$$

For both mechanisms, the ORR, OER and bifunctional overpotentials were calculated as [25,41]

$$\eta^{ORR} = |1.23 - U_{ORR}^{onset}| \quad (21)$$

$$\eta^{OER} = |1.23 - U_{OER}^{onset}| \quad (22)$$

$$\eta^{bifunc} = \eta^{ORR} + \eta^{OER} \quad (23)$$

3. Results and discussion

3.1. Structure and stability of DACs

Fig. 1a illustrates the structure models of studied MM′N_6-DACs. To simulate DACs with different curvature conditions, the planar state with zero curvature effect was represented by dual-atom sites anchored on nitrogen-doped graphene (i.e. $d = \infty$ nm, representing no curvature), and two curved conditions were represented by those on nitrogen-doped single-walled carbon nanotubes (CNTs) with two diameters(i.e. d = 1.3 nm representing smaller curvature, and d = 0.8 nm representing larger curvature) [38,41]. In this way, we have covered a wide range of curvatures.

Experimentally, the planar-state DACs can be synthesized by anchoring metal dimers on a carbon substrate such as graphene [55] or porous carbon [56], while the curved ones can be synthesized on curved carbon substrate such as a CNTs[57–59]. For example, FeCo DACs on two kinds of CNT substrates have been synthesized for ORR catalysis[58,59], and Ni_2 DACs on CNT substrate have been synthesized for electrochemical CO_2 reduction[57]. This indicates the feasibility of synthesizing DACs with surface curvature. In the future, more curved DACs may be synthesized, and curved DACs may be confirmed to have potential application in OER catalysis.

For DAC models with different N species and relative position, the stability of the model is strongly influenced by the local coordination environment of the metal dimers[60]. Here we focused on the most stable with lowest formation energy[60]. In this DAC model, each metal dimer is anchored by four pyridine nitrogen atoms and two

amino nitrogen atoms, denoted as $MM'N_6$-DACs (or MM′-DACs for brevity). We considered 8 transition metals (Fe, Co, Ni, Cu, Ru, Rh, Pd, or Pt) for the dual-metal sites, since they are common design choices for DACs for ORR and OER[34,55,61,62].

To examine the possibility of experimentally synthesizing these DACs and their electrochemical stability, we calculated their formation energy (E_{form}) and dissociation potential (U_{diss}) as follows[34,63],

$$E_{form} = (E_{DAC} - E_{N\text{-}C} - E_{M'} - E_M)/2 \quad (24)$$

$$U_{diss} = U^0_{diss}(\text{M-bulk}) - E_{form}/ne \quad (25)$$

E_{DAC} represents the total energy of the DACs and $E_{N\text{-}C}$ is total energy of the nitrogen-doped carbon substrate. Here $E_{M'}$ and E_M are the atomic energies of metals M and M′ in their most stable bulk state, respectively. U^0_{diss}(M-bulk) represents the standard dissolution potential of the bulk metals. And n is the number of electrons transferred during the dissolution[34].

If $E_{form} < 0$ eV, we regard the DAC as feasible to synthesize experimentally. When $U_{diss} > 0$, we regard the DAC is as electrochemically stable. Fig. 1b indicates the formation energy and dissolution potential of the DACs investigated. All proposed DACs have negative formation energies and positive dissolution potentials, suggesting they are synthetically feasible and electrochemically stable. Tables S1-S3 list the exact values of E_{form} and U_{diss} at the three curvature conditions.

3.2. ORR and OER activity of DACs

Fig. 2 compares two mechanisms of ORR and OER. In ORR, O_2 is reduced into water through four steps of electron-proton transfers, which can proceed through dissociative and associative mechanisms.

The four steps of ORR can be expressed as

- $O_2 \leftrightarrow *O + *OH \leftrightarrow 2*OH \leftrightarrow *OH \leftrightarrow H_2O$ in the dissociative mechanism
- $O_2 \leftrightarrow *OOH \leftrightarrow *O \leftrightarrow *OH \leftrightarrow H_2O$ in the associative mechanism.

By contrast, OER can be regarded as the reverse reaction of ORR where water is oxidized into O_2. More details about these two mechanisms are illustrated in Section 2.1. Most existing research on DACs considers their performance only for the associative mechanism. However, some recent studies show that oxygen electrocatalysis on DACs may instead involve the dissociative mechanism due to synergy of the dual atoms [34,43,44], suggesting that for DACs, the dissociative mechanism deserves more attention. Therefore, both mechanisms were considered in this study.

Fig. 3 exhibits theoretical activity, adsorption free energy and promising candidates of investigated DACs for mono- and bi-functional oxygen electrocatalysis in the two mechanisms. Exact values of adsorption free energies and overpotentials of all DACs are shown in Figure S1 and S2, respectively. The theoretical activity of all DACs is indicated in volcano plots (Fig. 3a-f) with the best candidates marked by stars. Here lower overpotential means higher catalytic activity. The three benchmarks for screening DACs candidates for ORR, OER, and bifunctional oxygen electrocatalysis were set as

ORR overpotential of Pt (111) (0.45 V),

OER overpotential of RuO_2 (110) (0.37 V), and

bifunctional overpotential (0.82 V), the summation of the two values. [25].

DACs with overpotential lower than these benchmarks are potential catalysts for the corresponding reactions in the oxygen electrode of rechargeable metal-air batteries.

By comparing the activity of the best DACs for mono- and bi-functional oxygen electrocatalysis in two mechanisms, we see that the dissociative mechanism allows identification DACs with ultra-high activity, because the best DACs in the dissociative

mechanism exhibit much higher activity than those in associative mechanism. In the dissociative mechanism, the best DACs for ORR, OER, and bi-functional oxygen electrocatalysis are

- $CoCu_{d=\infty\ nm}$-DAC (η^{ORR} = 0.09 V),
- $CoCu_{d=1.3\ nm}$-DAC (η^{OER} = 0.10 V), and
- $CoCu_{d=\infty\ nm}$-DAC (η^{bifunc} = 0.22 V).

as shown in Fig. 3a-c, Whereas in the associative mechanism, the best DACs for ORR, and OER and the two best DACs bi-functional oxygen electrocatalysis are

- $FeCo_{d=\infty\ nm}$-DAC (η^{ORR} = 0.26 V), and
- $RhFe_{d=0.8\ nm}$-DAC (η^{OER} = 0.26 V),
- $RhFe_{d=0.8\ nm}$-DAC (η^{bifunc} = 0.62 V)
- $CoNi_{d=1.3\ nm}$-DAC (η^{bifunc} = 0.62 V)

as shown in Fig. 3d-f.

To analyze whether the adsorption of intermediates conforms to the scaling relationship, a well-known bottleneck in developing high-performance oxygen electrocatalysts[34,64], we performed linear fitting for adsorption free energies of intermediates in both mechanisms. Interestingly, for the dissociative pathway, both $\Delta G_{*O/*OH}$ and $\Delta G_{*OH/*OH}$ exhibit a poor linear relationship with ΔG_{*OH}, with $R^2 \sim 0.4$, as shown in Fig. 3g. This indicates that the dissociative mechanism enables DACs to circumvent the scaling relationship between intermediates, which facilitates finding DACs with ultra-high activity for mono- and bi-functional oxygen electrocatalysis [34,43]. Whereas for the associative pathway, both ΔG_{*OOH} and ΔG_{*O} correlate strongly with ΔG_{*OH} in a linear manner, with $R^2 > 0.8$, as shown in Fig. 3h. This demonstrates that the adsorption of intermediates in the associative mechanism conforms to the scaling

relationship, which impedes finding of improved DACs candidates for oxygen-involving reactions.

Fig. 3i-k list the potential DACs at three curvature conditions for ORR, OER, and bifunctional oxygen electrocatalysis for both mechanisms. For ORR, Fig. 3i showcases 31 potential candidates in the dissociative mechanism and 30 ones in the associative mechanism. Among these candidates, $FeCo_{d=\infty\ nm}$ exhibit excellent ORR activity in both mechanisms (η^{ORR} = 0.26 V), in line with [55]experimental [65] and other theoretical [60] results, since the limiting step in both mechanisms is *OH $\rightarrow$ H_2O. It should be noted that 4 candidates exhibit superior ORR activity in the dissociative mechanism with η^{ORR} below 0.2 eV:

- $CoCu_{d=\infty\ nm}$ (0.09 V),
- $CoCo_{d=1.3\ nm}$ (0.16 V),
- $NiRh_{d=0.8\ nm}$ (0.13 V),
- $CuRh_{d=0.8\ nm}$ (0.19 V).

For OER, Fig. 3j exhibits 21 potential candidates in the dissociative mechanism and 15 in the associative mechanism. $CoNi_{d=\infty\ nm}$-DAC is a promising OER catalyst in both mechanisms, especially in associative mechanism (η^{OER} = 0.27 V), which is in line with experimental result that atomically dispersed Co/Ni dual sites anchored on nitrogen-doped carbon exhibits a low η^{OER} of 0.25 V at 10 mA cm^{-2}[66]. We note here that 3 candidates exhibit superior ORR activity in the dissociative mechanism with η^{OER} below 0.2 eV:

- $CoCu_{d=\infty\ nm}$ (0.13 V),
- $CoCu_{d=1.3\ nm}$ (0.10 V), and
- $RhRh_{d=0.8\ nm}$ (0.19 V).

For bifunctional oxygen electrocatalysis, Fig. 3k lists 22 promising candidates in the dissociative mechanism and 16 in the associative mechanism. We note that 4 candidates exhibit superior ORR activity in the dissociative mechanism with η^{bifunc} below 0.4 eV:

- $CoCu_{d=\infty\ \text{nm}}$ (0.22 V),
- $CoCu_{d=1.3\ \text{nm}}$ (0.32 V),
- $CoCo_{d=1.3\ \text{nm}}$ (0.36 V), and
- $NiRh_{d=0.8\ \text{nm}}$ (0.34 V).

For both mechanisms, we found DACs with ORR/OER overpotential lower than 0.30 V, the theoretical minimum for SACs, suggesting the superiority of DACs over SACs for oxygen electrocatalysis. Our screening provides many candidates for mono- and bi-functional oxygen electrocatalysis in rechargeable metal-air batteries. The excellent candidates with low ORR overpotential can facilitate feasible discharging in rechargeable metal-air batteries, while those with low OER overpotential allow for smooth charging. And those with low bifunctional overpotential can act as bifunctional catalysts to accelerate reactions in discharging and charging cycle.

3.3. Oxygen electrocatalysis on CoCu DACs

In the planar state, $CoCuN_6$-DAC exhibits superior activity for mono- and bi-functional oxygen electrocatalysis in dissociative mechanism (η^{ORR} = 0.09 V, η^{OER} = 0.13 V, and η^{bifunc} = 0.22 V) as shown in Fig. 4a, which is much better than that of CoN_4-SAC and CuN_4-SAC in both the associative and dissociative mechanisms as shown in Table S4. This indicates the superiority of DACs for oxygen electrocatalysis over SACs. Moreover, for planar-state DACs, the activity of $CoCuN_6$ in the dissociative mechanism is better than $CoCoN_6$ and $CuCuN_6$ in both the associative and dissociative mechanisms as shown in Table S4, which suggests that synergy between heterogeneous

Co and Cu atoms is better than their homogeneous counterparts. In addition, the hydrogen adsorption free energy (ΔG_{*H}) on planar-state $CoCuN_6$-DAC is 0.64 eV, indicating that HER activity on this DAC is quite low, making HER an unlikely competitive reaction to ORR[67].

Three $CoCuN_6$-DACs were selected to understand the curvature effects on DACs for oxygen electrocatalysis in the dissociative mechanism based on the following two reasons: first, all three CoCu-DACs at different curvature conditions are potential candidates for bifunctional oxygen electrocatalysis as shown in Fig. 3k. Moreover, $CoCu_{d=\infty\ nm}$-DAC (η^{ORR} = 0.09 V) and $CoCu_{d=1.3\ nm}$-DAC (η^{OER} = 0.10 V) are the optimal candidates for ORR and OER, respectively. As shown in Fig. 4b and Fig. S4, the adsorption free energies of all intermediates in the whole dissociative pathway gradually decrease with increasing curvature from $d = \infty$ nm to d = 0.8 nm, suggesting that the adsorption strength of these intermediates increases with curvature[43]. On $CoCu_{d=\infty\ nm}$-DAC, the adsorption free energies of all intermediates are close to zero, leading to its superb activity for mono- and bi-functional oxygen electrocatalysis, with η^{ORR} = 0.09 V, η^{OER} = 0.13 V, and η^{bifunc} = 0.22 V. The rate-limiting step for ORR on $CoCu_{d=\infty\ nm}$-DAC is *O + *OH → 2*OH, while that for OER is H_2O → *OH. On $CoCu_{d=1.3\ nm}$-DAC, η^{OER} is smaller while η^{ORR} and η^{bifunc} are larger than those on $CoCu_{d=\infty\ nm}$-DAC, with η^{OER} = 0.10 V, η^{ORR} = 0.22 V, η^{bifunc} = 0.32 V. The rate-limiting step for ORR on $CoCu_{d=1.3\ nm}$-DAC is *OH → H_2O, while that for OER is 2*OH → *O/*OH. On $CoCu_{d=0.8\ nm}$, all three overpotentials are largest among studied $CoCuN_6$-DACs, with η^{ORR} = 0.39 V, η^{OER} = 0.40 V, η^{bifunc} = 0.80 V. The rate-limiting step for ORR on $CoCu_{d=0.8\ nm}$-DAC is *OH → H_2O, while that for OER is *O/*OH → O_2.

To understand the electronic origin of the gradually strengthened adsorption on $CoCuN_6$-DACs with increasing curvature, the projected density of states (pDOS) of related atomic orbitals were compared before and after the adsorption of OH

intermediate, as shown in Fig. 4c-h. OH intermediate is chosen for analysis of the electronic properties, since it is the common intermediate in two mechanisms. For three CoCu-DACs, main peaks of the *p* orbitals of O atoms overlap well with the *d* orbitals of Co atoms, suggesting that O atoms bond to Co atoms in three systems, in line with the relaxed structures where O bonds with Co. Compared with $CoCu_{d=\infty\ nm}$-DAC, the *d* orbitals of the Co atoms in $CoCu_{d=1.3\ nm}$-DAC and $CoCu_{d=0.8\ nm}$-DAC have more electronic states near the Fermi level, which facilitates electron transfer between Co and O in DACs on CNT substrates, leading to stronger adsorption of *OH on $CoCu_{d=1.3\ nm}$-DAC and $CoCu_{d=0.8nm}$-DAC. As for the *d* orbitals of the Cu atoms, $CoCu_{d=1.3\ nm}$-DAC and $CoCu_{d=0.8\ nm}$-DAC also have more electronic states near the Fermi level than $CoCu_{d=\infty\ nm}$-DAC. This allows stronger adsorption of *O/*OH and *2OH on two curved CoCu-DACs than planar $CoCu_{d=\infty\ nm}$-DAC, since adsorption of intermediates in these two steps involving both Co and Cu atoms. This indicates that tensile strain from curvature effects increases the electronic states of the metal atom near the Fermi level, which enhances the adsorption of intermediates.

4. Conclusion

Summarizing, we employed DFT calculations to investigate the stability and electrocatalytic activity for two mechanisms on curved DACs effects for mono- and bi-functional oxygen electrocatalysis. We found that all studied DACs have negative formation energies and positive dissolution potentials, suggesting their synthetical feasibility and electrochemical stability.

We found some promising catalysts with ultra-high predicted activity in the dissociative mechanism for both mono- and bi-functional oxygen electrocatalysis:

- $CoCu_{d=\infty\ nm}$-DAC (with $\eta^{ORR} = 0.09$ V, $\eta^{OER} = 0.13$ V, and $\eta^{bifunc} = 0.22$ V) and
- $CoCu_{d=1.3\ nm}$-DAC (with $\eta^{ORR} = 0.22$ V, $\eta^{OER} = 0.10$ V, and $\eta^{bifunc} = 0.32$ V).

These studies suggest many potential candidates for oxygen electrocatalysis in rechargeable metal-air batteries, fuel cells, and electrolyzer.

In addition, we demonstrated that in the dissociative mechanism, the scaling relationship between intermediates in oxygen electrocatalysis is broken; while in associative mechanism, this scaling relationship limits the catalysts activity. Traditionally, only associative mechanism has usually been considered for oxygen electrocatalysis on dual-atom catalysts, with the possible synergy between two active sites neglected, which we show is an oversight. Thus, we show that for the dissociative mechanisms, the synergy between two active sites can break the scaling relationship between intermediates in oxygen electrocatalysis, leading to catalysts with extremely high activity.

Moreover, we found that using CNT to increase the curvature from $d = \infty$ nm to $d = 0.8$ nm, gradually strengthens the adsorption of all intermediates on $CoCuN_6$-DACs. By comparing the partial DOS around the Fermi level of related systems, we found that the enhanced adsorption results increased electronic states of metal atoms near the Fermi level.

Declaration of Competing Interest

The authors declare that they have no known competing financial interests or personal relationships that could have appeared to influence the work reported in this paper.

Data availability

Data will be available on request.

Acknowledgements

G.H.C. acknowledges financial support from the General Research Fund (Grant No. 17309620) and Hong Kong Quantum AI Lab, AIR@InnoHK of the Hong Kong Government. W.A.G. thanks the U.S. National Science Foundation (CBET- 2311117) for support.

Supporting Information

The SI includes the detailed mechanisms of ORR and OER, including the formation energy and dissolution potential of all DACs, as well as adsorption free energies and overpotentials on all DACs and related SACs.

References

1 R. Cao, J.-S. Lee, M. Liu and J. Cho, *Adv Energy Mater*, 2012, **2**, 816–829.

2 C. Wei, R. R. Rao, J. Peng, B. Huang, I. E. L. Stephens, M. Risch, Z. J. Xu and Y. Shao-Horn, *Advanced Materials*, 2019, **31**, 1806296.

3 J. Fu, Z. P. Cano, M. G. Park, A. Yu, M. Fowler and Z. Chen, *Advanced Materials*, 2017, **29**, 1604685.

4 I. Katsounaros, S. Cherevko, A. R. Zeradjanin and K. J. J. Mayrhofer, *Angewandte Chemie International Edition*, 2014, **53**, 102–121.

5 K. Jiao, J. Xuan, Q. Du, Z. Bao, B. Xie, B. Wang, Y. Zhao, L. Fan, H. Wang, Z. Hou, S. Huo, N. P. Brandon, Y. Yin and M. D. Guiver, *Nature*, 2021, **595**, 361–369.

6 B. G. Pollet, S. S. Kocha and I. Staffell, *Curr Opin Electrochem*, 2019, **16**, 90–95.

7 Y. Jiao, Y. Zheng, M. Jaroniec and S. Z. Qiao, *Chem Soc Rev*, 2015, **44**, 2060–2086.

8 J. Wu and H. Yang, *Acc Chem Res*, 2013, **46**, 1848–1857.

9 M. Escudero-Escribano, P. Malacrida, M. H. Hansen, U. G. Vej-Hansen, A. Velázquez-Palenzuela, V. Tripkovic, J. Schiøtz, J. Rossmeisl, I. E. L. Stephens and I. Chorkendorff, *Science (1979)*, 2016, **352**, 73–76.

10 J. H. Montoya, L. C. Seitz, P. Chakthranont, A. Vojvodic, T. F. Jaramillo and J. K. Nørskov, *Nat Mater*, 2017, **16**, 70–81.

11 Y. Lee, J. Suntivich, K. J. May, E. E. Perry and Y. Shao-Horn, *J Phys Chem Lett*, 2012, **3**, 399–404.

12 A. Wang, J. Li and T. Zhang, *Nat Rev Chem*, 2018, **2**, 65–81.

13 S. Mitchell and J. Pérez-Ramírez, *Nat Commun*, 2020, **11**, 4302.

14 C. Zhu, S. Fu, Q. Shi, D. Du and Y. Lin, *Angewandte Chemie International Edition*, 2017, **56**, 13944–13960.

15 Y. Wang, D. Wang and Y. Li, *Advanced Materials*, 2021, **33**, 2008151.

16 Q. Zhang and J. Guan, *Adv Funct Mater*, 2020, **30**, 2000768.

17 A. Wang, J. Li and T. Zhang, *Nat Rev Chem*, 2018, **2**, 65–81.

18 S. Mitchell and J. Pérez-Ramírez, *Nat Commun*, 2020, **11**, 4302.

19 R. Li and D. Wang, *Adv Energy Mater*, 2022, **12**, 2103564.

20 M. Tamtaji, M. G. Kim, Z. Li, S. Cai, J. WANG, P. R. Galligan, F.-F. Hung, H. Guo, S. Chen, Z. Luo, W. Wu, W. A. Goddard and G. Chen, *Nano Energy*, 2024, 109634.

21 H. Shang, X. Zhou, J. Dong, A. Li, X. Zhao, Q. Liu, Y. Lin, J. Pei, Z. Li, Z. Jiang, D. Zhou, L. Zheng, Y. Wang, J. Zhou, Z. Yang, R. Cao, R. Sarangi, T. Sun, X. Yang, X. Zheng, W. Yan, Z. Zhuang, J. Li, W. Chen, D. Wang, J. Zhang and Y. Li, *Nat Commun*, 2020, **11**, 3049.

22 L. Peng, L. Shang, T. Zhang and G. I. N. Waterhouse, *Adv Energy Mater*, 2020, **10**, 2003018.

23 C. Wan, X. Duan and Y. Huang, *Adv Energy Mater*, 2020, **10**, 1903815.

24 J. Zhang, H. Yang and B. Liu, *Adv Energy Mater*, 2021, **11**, 2002473.

25 Y. Li, Y. Feng, D. Zheng, X. Zhao, Y. Zhou, X. Fu and X. Chen,

Chemical Engineering Journal, 2023, **476**, 146753.

26 M. Tamtaji, M. G. Kim, J. WANG, P. R. Galligan, H. Zhu, F.-F. Hung, Z. Xu, Y. Zhu, Z. Luo, W. A. Goddard and G. Chen, *Advanced Science*, 2024, **n/a**, 2309883.

27 Y. Pang, C. Su, L. Xu and Z. Shao, *Prog Mater Sci*, 2023, **132**, 101044.

28 M. Li, H. Wang, W. Luo, P. C. Sherrell, J. Chen and J. Yang, *Advanced Materials*, 2020, **32**, 2001848.

29 T. Wang, Q. Zhao, Y. Fu, C. Lei, B. Yang, Z. Li, L. Lei, G. Wu and Y. Hou, *Small Methods*, 2019, **3**, 1900210.

30 Y. Wang, Y. Liu, W. Liu, J. Wu, Q. Li, Q. Feng, Z. Chen, X. Xiong, D. Wang and Y. Lei, *Energy Environ Sci*, 2020, **13**, 4609–4624.

31 Y. Chen, J. Lin, Q. Pan, X. Liu, T. Ma and X. Wang, *Angewandte Chemie International Edition*, 2023, **62**, e202306469.

32 R. Li and D. Wang, *Adv Energy Mater*, 2022, **12**, 2103564.

33 Y. Ying, X. Luo, J. Qiao and H. Huang, *Adv Funct Mater*, 2021, **31**, 2007423.

34 C. Fang, J. Zhou, L. Zhang, W. Wan, Y. Ding and X. Sun, *Nat Commun*, 2023, **14**, 4449.

35 L. Zhao, S. Guo, H. Liu, H. Zhu, S. Yuan and W. Guo, *ACS Appl Nano Mater*, 2018, **1**, 6258–6268.

36 Q. Xu, H. Li, Y. Shi, Z. Bi and Y. Wu, *ACS Appl Nano Mater*, 2021, **4**, 600–611.

37 H. Liu, L. Zhao, Y. Liu, J. Xu, H. Zhu and W. Guo, *Catal Sci Technol*,

2019, **9**, 5301–5314.

38 S. Yuan, G. Meng, D. Liu, W. Zhao, H. Zhu, Y. Chi, H. Ren and W. Guo, *ACS Appl Mater Interfaces*, 2022, **14**, 52544–52552.

39 W. Liu, K. Guo, Y. Xie, S. Liu, L. Chen and J. Xu, *Sci Rep*, 2023, **13**, 9926.

40 G. Han, X. Zhang, W. Liu, Q. Zhang, Z. Wang, J. Cheng, T. Yao, L. Gu, C. Du, Y. Gao and G. Yin, *Nat Commun*, 2021, **12**, 6335.

41 X. Zhou, Z. Jin, J. Zhang, K. Hu, S. Liu, H.-J. Qiu and X. Lin, *Nanoscale*, 2023, **15**, 2276–2284.

42 J. Wang, N. Li, Y. Jiang, H. Sheng and M. Sun, *Appl Surf Sci*, 2024, **658**, 159858.

43 R. Cepitis, N. Kongi, J. Rossmeisl and V. Ivaništšev, *ACS Energy Lett*, 2023, **8**, 1330–1335.

44 J. Liu, H. Xu, J. Zhu and D. Cheng, *JACS Au*, 2023, **3**, 3031–3044.

45 J. P. Perdew, K. Burke and M. Ernzerhof, *Phys Rev Lett*, 1996, **77**, 3865–3868.

46 G. Kresse and J. Furthmüller, *Comput Mater Sci*, 1996, **6**, 15–50.

47 G. Kresse and J. Furthmüller, *Phys Rev B*, 1996, **54**, 11169–11186.

48 G. Kresse and D. Joubert, *Phys Rev B*, 1999, **59**, 1758–1775.

49 S. Grimme, *J Comput Chem*, 2006, **27**, 1787–1799.

50 S. Grimme, J. Antony, S. Ehrlich and H. Krieg, *J Chem Phys*, 2010, **132**, 154104.

51 K. Mathew, R. Sundararaman, K. Letchworth-Weaver, T. A. Arias

and R. G. Hennig, *J Chem Phys*, 2014, **140**, 084106.

52 K. Mathew, V. S. C. Kolluru, S. Mula, S. N. Steinmann and R. G. Hennig, *J Chem Phys*, 2019, **151**, 234101.

53 A. Cao and J. K. Nørskov, *ACS Catal*, 2023, **13**, 3456–3462.

54 J. K. Nørskov, J. Rossmeisl, A. Logadottir, L. Lindqvist, J. R. Kitchin, T. Bligaard and H. Jónsson, *J Phys Chem B*, 2004, **108**, 17886–17892.

55 M. Tamtaji, Q. Peng, T. Liu, X. Zhao, Z. Xu, P. R. Galligan, M. D. Hossain, Z. Liu, H. Wong, H. Liu, K. Amine, Y. Zhu, W. A. Goddard III, W. Wu and Z. Luo, *Nano Energy*, 2023, **108**, 108218.

56 J. Wang, Z. Huang, W. Liu, C. Chang, H. Tang, Z. Li, W. Chen, C. Jia, T. Yao, S. Wei, Y. Wu and Y. Li, *J Am Chem Soc*, 2017, **139**, 17281–17284.

57 X.-M. Liang, H.-J. Wang, C. Zhang, D.-C. Zhong and T.-B. Lu, *Appl Catal B*, 2023, **322**, 122073.

58 L.-L. Liu, M. ul Haq, L. Zhang, J.-J. Feng, L. Wu and A.-J. Wang, *Journal of Electroanalytical Chemistry*, 2023, **951**, 117953.

59 J. Wang, W. Liu, G. Luo, Z. Li, C. Zhao, H. Zhang, M. Zhu, Q. Xu, X. Wang, C. Zhao, Y. Qu, Z. Yang, T. Yao, Y. Li, Y. Lin, Y. Wu and Y. Li, *Energy Environ Sci*, 2018, **11**, 3375–3379.

60 Y. Meng, C. Yin, K. Li, H. Tang, Y. Wang and Z. Wu, *ACS Sustain Chem Eng*, 2019, **7**, 17273–17281.

61 Y. Meng, Y. Gao, K. Li, H. Tang, Y. Wang and Z. Wu, *The Journal of Physical Chemistry C*, 2020, **124**, 9142–9150.

62 Y. Meng, C. Yin, K. Li, H. Tang, Y. Wang and Z. Wu, *ACS Sustain Chem Eng*, 2019, **7**, 17273–17281.

63 F. Rehman, S. Kwon, C. B. Musgrave, M. Tamtaji, W. A. Goddard and Z. Luo, *Nano Energy*, 2022, **103**, 107866.

64 J. Pérez-Ramírez and N. López, *Nat Catal*, 2019, **2**, 971–976.

65 J. Wang, Z. Huang, W. Liu, C. Chang, H. Tang, Z. Li, W. Chen, C. Jia, T. Yao, S. Wei, Y. Wu and Y. Li, *J Am Chem Soc*, 2017, **139**, 17281–17284.

66 Z. Pei, X. F. Lu, H. Zhang, Y. Li, D. Luan and X. W. (David) Lou, *Angewandte Chemie International Edition*, 2022, **61**, e202207537.

67 M. Tamtaji, Y. Li, Y. Cai, H. Liu, W. A. Goddard III and G. Chen, *J Mater Chem A Mater*, 2023, **11**, 25410–25421.

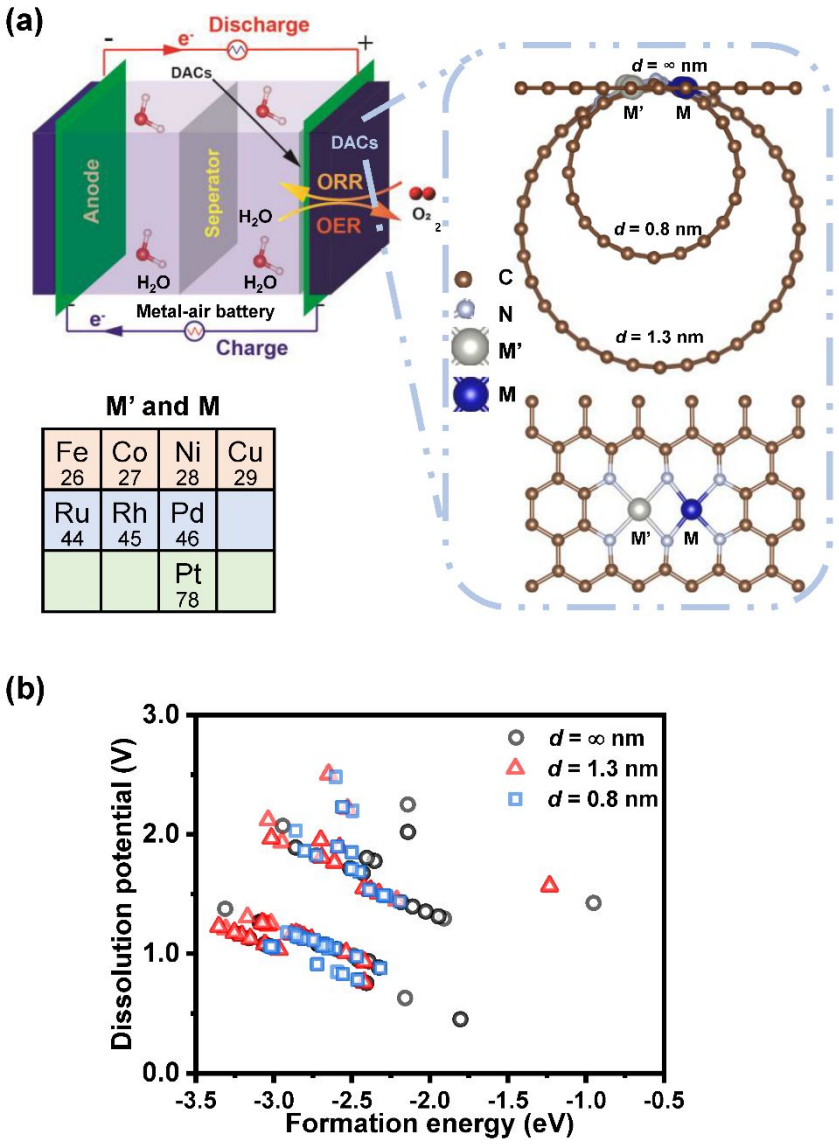

Fig. 1. Schematics and stability of studied DACs. (a) Schematics for $MM'N_6$-DACs at different curvature for electrocatalyzing ORR and OER. Each metallic dimer MM′ is anchored by 6 nitrogen atoms in N-doped graphene ($d = \infty$ nm) and N-doped carbon nanotubes ($d = 1.3$ nm and $d = 0.8$ nm). For each metal site, 8 transition metals are considered: Fe, Co, Ni, Cu, Ru, Rh, Pd, or Pt. Atom labels: O (red), H (pink), C(brown), N (light blue), M′ (gray) and M (dark blue). (b) Formation energy and dissolution potential of studied DACs.

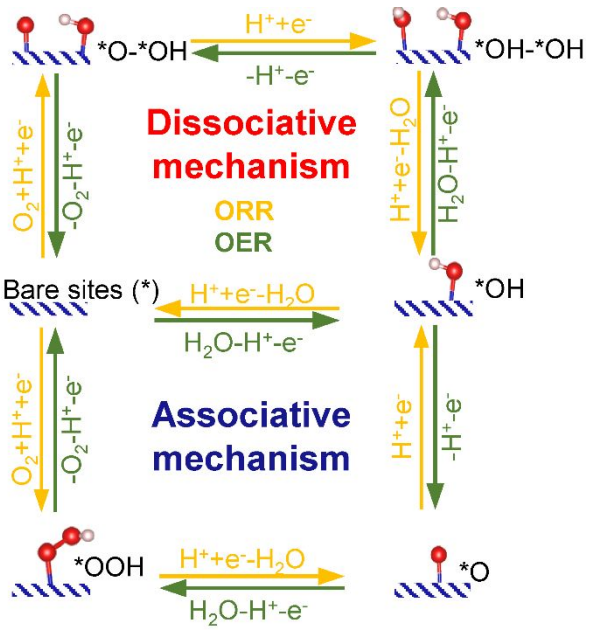

Fig. 2. Two reaction mechanisms for ORR and OER. Yellow color represents the reaction pathway of ORR, while green color represents the reaction pathway of OER.

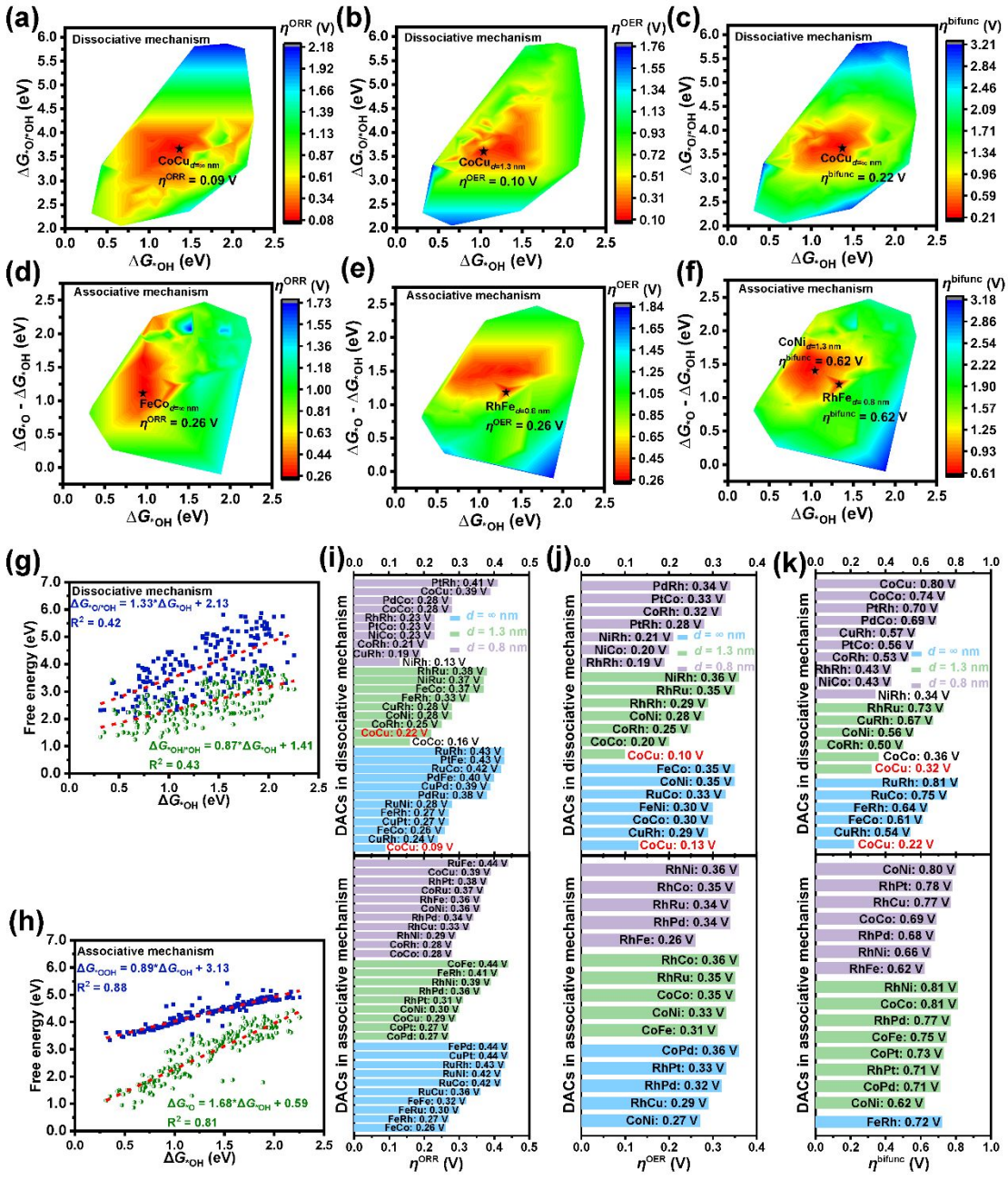

Fig. 3. Theoretical oxygen electrocatalyzing activity of DACs in this study. In dissociative mechanism, ORR overpotential (a), OER overpotential (b), and bifunctional overpotential (c). In associative mechanism, ORR overpotential (d), OER overpotential (e), and bifunctional overpotential (f). The stars in overpotential graphs mark the DACs with the highest activity in this study. The fitting of Gibbs free energy between 3 intermediates in dissociative mechanism (g) and associative mechanism (h). The red dash lines represent the linear fitting of Gibbs free energy between

intermediates. Potential DACs candidates with overpotential lower than the benchmarks for ORR (i), OER (j), and bifunctional catalysis (k), respectively. The three benchmarks are 0.45 V, 0.37 V, 0.82 V, respectively.

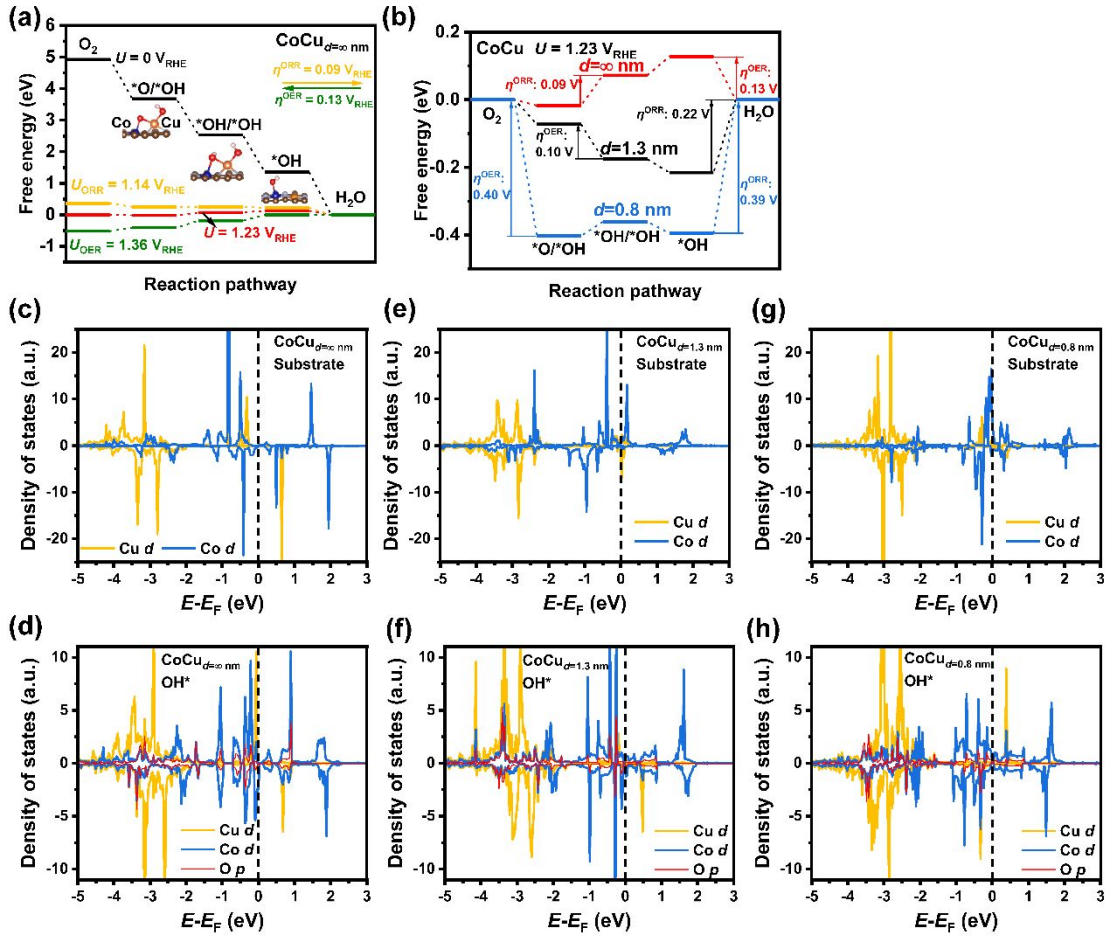

Fig. 4. Theoretical activity and electronic structures of $CoCuN_6$-DACs at different curvature. (a) Gibbs free energy diagram for $CoCuN_6$-DAC at the planar state in dissociative mechanism. The adsorption configurations of intermediates at each step are shown under the step. (b) Gibbs free energy diagram for $CoCuN_6$-DACs at different curvature in dissociative mechanism. The partial density of states (pDOS) of $CoCuN_6$-DAC without curvature before (c) and after (d) the adsorption of OH intermediate. PDOS of $CoCuN_6$-DAC in 1.3 nm CNT before (e) and after (f) the adsorption of OH intermediate. PDOS of $CoCuN_6$-DAC in 0.8 nm CNT before (g) and after (h) the adsorption of OH intermediate. The black dash line in pDOS represents the

Fermi level.

Data availability

The data supporting this article have been included as part of the Supplementary Information.